Cellulose
DOI 10.1007/s10570-015-0788-7

ORIGINAL PAPER

Probing crystallinity of never-dried wood cellulose with Raman spectroscopy

Umesh P. Agarwal · Sally A. Ralph · Richard S. Reiner · Carlos Baez

Received: 13 April 2015 / Accepted: 16 October 2015

Abstract The structure of wood cell wall cellulose in its native state remains poorly understood, limiting the progress of research and development in numerous areas, including plant science, biofuels, and nanocellulose based materials. It is generally believed that cellulose in cell wall microfibrils has both crystalline and amorphous regions. However, there is evidence that appears to be contrary to this assumption. Here we show, using 1064-nm FT-Raman spectroscopy, that (1) compared to the crystalline state, cellulose in the never-dried native state is laterally aggregated but in a less-than crystalline state wherein internal chains are water-accessible, (2) hydroxymethyl groups (CH_2OH) in cellulose exist not only in the *tg* conformation but also in the *gt* rotamer form, and (3) in native-state fibrils, low-frequency Raman bands due to cellulose crystal domains are absent, indicating the lack of crystallinity. Further evidence of the absence of crystallinity of the fibrils was the failure of the normal 64 % H_2SO_4 hydrolysis procedure to produce nanocellulose crystals from untreated wood. X-ray diffraction data obtained on wood, treated-wood, and wood-cellulose samples were consistent with the new finding and indicated that full-width-at-half-height of the X-ray diffractograms and lateral disorder in samples as measured by Raman were correlated ($R^2 = 0.95$).

Keywords Plant cell wall · Cellulose structure · Crystallinity · Microfibril · Nanocellulose · Raman spectroscopy · X-ray diffraction

Introduction

Knowledge of native cell wall cellulose structure is critical for making advances in a number of fields. For example, further elucidation of structure will contribute to understanding cellulose biosynthesis, plant growth, and function in the cell wall (Cosgrove 2005). In the area of biofuels, before cellulose can be converted to glucose and fermented to ethanol or other chemicals, the cell wall must be deconstructed. It is widely held that cellulose ultrastructure plays a central role (Ragauskas et al. 2006; Sun et al. 2014) in the deconstruction process, and to expedite cell wall deconstruction, the cellulose structure is altered by different pretreatments (Langan et al. 2014; Sun et al. 2014). A more clear view of the structure before and after the treatment would be valuable. Similarly, production of novel composites from nanocellulose (Moon et al. 2011) is an area that will benefit from such advanced understanding. Although the

Electronic supplementary material The online version of this article (doi:10.1007/s10570-015-0788-7) contains supplementary material, which is available to authorized users.

U. P. Agarwal (✉) · S. A. Ralph · R. S. Reiner · C. Baez
Fiber and Chemical Sciences Research, USDA FS, Forest Products Laboratory, 1 Gifford Pinchot Drive, Madison, WI 53726-2398, USA
e-mail: uagarwal@fs.fed.us

Published online: 24 October 2015

crystallinities of same-source derived cellulose nanocrystals and cellulose nanofibrils (CNCs and CNFs, respectively) differ significantly (Xu et al. 2013) there is little understanding of these differences.

This situation of insufficient knowledge of the structure is not due to lack of effort of researchers but rather a consequence of limitations of analytical methods to investigate cell wall structure in situ (Martínez-Sanz et al. 2015). Most analytical methods require isolation and purification of the cellulose. These steps usually involve thermochemical treatments that can result in the modification of the cellulose native structure. Nevertheless, numerous methods have been applied to investigate the native state of cell walls and some information on cellulose structure has been obtained. Such methods include optical microscopy (Preston 1974), SEM (Donaldson 2007), TEM (Donaldson 2007), AFM (Ding and Himmel 2006), SNOM (Keplinger et al. 2014), X-ray diffraction (Liu et al. 2013; Newman et al. 2013; Thomas et al. 2014), neutron scattering (Thomas et al. 2014), IR (Largo-Gosens et al. 2014), Raman spectroscopy (Agarwal 2006, 2014; Agarwal et al. 2010; Gierlinger et al. 2010), SFG (vibrational sum frequency generation, Lee et al. 2014), and NMR spectroscopy (Newman 1999; Newman et al. 2013). For example, using confocal Raman spectroscopy (Agarwal 2006) Gierlinger et al. (2010) found that the secondary cell wall fibrils of the woody tissue were oriented at specific angles to the longitudinal axis of the fiber in never-dried samples. A comprehensive, multidisciplinary study (Fernandes et al. 2011) of the nanostructure of cellulose in spruce wood microfibrils favored a 24-chain model of the microfibril, and the researchers commented on the locations of the disordered regions. The researchers also considered an 18-chain model and found that the model would fit the small angle neutron scattering (SANS) data but not the WAXS data. However, their analysis assumed that the microfibrils were partly crystalline—a traditional approach. Nevertheless, Jarvis (2013 and papers cited therein) reviewed the studies published subsequent to his 2011 paper and came to the conclusion that the 36-chain microfibril models can be completely ruled out and the best microfibril model consists of irregularly shaped 18-chain microfibrils. A large part of Jarvis's (2013) reasoning was based on the work of Newman et al. (2013) whose work focused on XRD and ^{13}C NMR investigations of mung bean primary cell walls. These researchers tested various models of cellulose chains packing, including disordered cellulose chains inside microfibrils, and came to the conclusion that good fits of the simulations to both XRD and NMR data were obtained for collections of 18-chain models (disordered or not) with mixed cross-sectional shapes and occasional linking of the microfibrils (Newman et al. 2013). Moreover, the authors made the statement that "cellulose microfibrils are not crystalline, in the strict definition of that word". On the other hand, based on AFM measurements in water, Kuramae et al. (2014) found that the width and height of the TEMPO (2,2,6,6-tetramethylpiperidine-1-oxyl)-oxidized plant cellulose microfibrils were ~ 3 nm in each cross-sectional dimensions and these measurements agreed with those estimated based on the X-ray diffraction. Moreover, they reported that the air dried microfibrils had the reduced width of 2 nm. A microfibril that has a cross-section of 3 nm in native state is likely to consist of 36 (6×6) chains of cellulose (Okita et al. 2010). Additionally, similar size measurements were also reported by Reza et al. (2014) who using a high resolution cryo-TEM found that in never-dried Norway spruce cell walls the average width of the microfibrils was 3.5 nm. In any case, it appears that if 18 chains were to be present in a 3–3.5 nm fibril then the average distance between cellulose chains, d[200], is likely to be larger than the usually reported 0.39 nm (French and Santiago Cintron 2013). And therefore, significant disorder is implied. It is important to note that Newman et al. (2013) further commented that to match the experimental diffractograms it was possible to incorporate unrealistically high levels of correlated disorder but that model would have required larger number of interior chains than estimated based on the NMR spectra of mung bean cell walls (Newman et al. 2013; Bootten et al. 2004). The estimated number of interior chains depends upon not only how the area at 89 ppm (C4 peak) is calculated but how the spectra are generated. Newman et al. (2013), obtained NMR spectra by using proton spin relaxation-editing technique (PSRE, Bootten et al. 2004) where the relaxation of the protons was allowed to occur for a particular period prior to the cross-polarization step in the CP/MAS protocol. However, this technique may have some problems as discussed by Atalla and VanderHart (1999). The overall effect being that the number of estimated interior chains could be inaccurate.

Consequently, that would open up the possibility of models that have more than 18 chains. Noteworthy is also the fact that compared to the mung bean cell walls crystallinity of wood has been reported to be much higher [37 % for mung bean (Newman et al. 2013) vs. 50 % for woods (Wikberg and Maunu 2004), both by ^{13}C NMR]. In these investigations, crystallinity was calculated based on the number of interior chains in the cellulose microfibril.

It is clear from past work and the recently published review (Martínez-Sanz et al. 2015) that non-crystalline cellulose means absence of crystals and presence of disorder implies accessibility of cellulose molecules to water. These characteristics are retained in the present investigation. Noteworthy is also that International Union of Crystallography considers a material crystalline if it has essentially a sharp diffraction pattern (http://reference.iucr.org/dictionary/Crystal).

Although visible-Raman spectroscopy has been used in the past to study cellulose (Atalla and Agarwal 1985; Atalla and Isogai 2005), 1064-nm FT-Raman spectroscopy provides spectra that have significantly better signal to noise (S/N) ratios, lower levels of sample fluorescence, and it allows study of Raman modes in the low frequency (LF) region (Agarwal 2014; Agarwal et al. 2013a; Hendra et al. 1991). Sampling in water and D_2O allows investigating cellulose in the never-dried state. Moreover, new understandings developed while interpreting the cellulose Raman spectra and spectral changes are key to making progress for understanding the structures of cellulose (Agarwal 2014; Agarwal et al. 2010, 2013a; Wiley and Atalla 1987).

In this study, we investigated a hardwood (aspen) and three softwoods (red pine, Douglas fir, and loblolly pine). Where necessary, other types of pure cellulose and pulp samples were also analyzed.

Materials and methods

Chemicals, celluloses, and pulps

Unless stated otherwise, all chemicals and reagents were purchased from Sigma-Aldrich (St. Louis, MO).

BNSWKP (Table 1, SA17, bleached northern softwood kraft pulp) was obtained from NIST (Reference materials 8495, National Institute of Standards and Technology, Gaithersburg, MD). Bacterial cellulose was produced by other researchers of our research group. Tunicate and *Cladophora* celluloses (Table 2, SA18; Table 2, SA24, respectively) were gifts from Dr. Akira Isogai (Tokyo University, Tokyo). Avicel PH-101 (Table 2, SA21) was from FMC Corporation (Newark, Delaware), and Whatman CC-31 powder (Table 2, SA22) was from Whatman International Ltd., (Maidstone, UK). Amorphous cellulose (Table 2, SA19) was generated by grinding Whatman CC-31 in a vibratory mill using steel balls for 120 min. The process has been described earlier (Agarwal et al. 2010).

Woods, preparation of delignified wood cell walls, and NaOH treatment

Hardwood Aspen (*Populous tremuloides*) and all softwoods (red pine, *pinus resinosa*; Douglas fir, *Pseudotsuga menziesii*; loblolly pine, *Pinus taeda* L.) were obtained from researchers at the Forest Products Laboratory (FPL). The aspen (SA1 in Table 1) and red pine (SA6 in Table 1) samples were delignified at room temperature using a procedure similar to that of Atalla et al. (2014). Shavings from ~5 g (1 × 1 × 5 cm sticks) of never-dried frozen red pine (annual rings 5, 6 and 7 from a 16 cm disc) and 135 ml of water were placed in a 250 ml Erlenmeyer flask along with a magnetic stir bar. 6.1 g of $NaClO_2$ were added and the pH brought to 4 with ~4 ml of acetic acid. The flask was loosely capped with an upturned glass beaker and was left to stir at room temperature. For next 5 weeks, weekly, the solution was decanted and water and fresh charges were added. Aspen wood sticks were treated in a similar fashion. The sample was taken from the 5 to 7 annual ring area from a disc of ~15 cm diameter; it had an estimated dry weight of 3.5 g. Both the red pine and aspen samples were each filtered and the retentate washed until the filtrate was of neutral pH. Both samples were then treated with 4 % NaOH solution, stirring for 72 h at RT. These were then filtered and washed until the filtrate was just below pH 7. In Table 2, these samples are described as SA2-ND and SA7-ND and represent never dried aspen and red pine cell walls, respectively.

HCl and TEMPO treated SA2-ND

A 10 ml sample of thawed SA2-ND aspen sample suspension was concentrated by drawing off as much

Table 1 Chemical composition (%) of various samples

Sample ID	Description	Klason lignin	Arabinan	Galactan	Glucan	Xylan	Mannan	Hemicellulose[a]
SA1	Aspen-wood, control	19.4	0.4	0.7	44.2	16.7	2.2	20.0
SA2	NaOH treated aspen wood holocellulose	1.6	0.1	0.3	73.0	6.6	3.5	10.5
SA3	HCl treated SA2, 8 h @ 25 °C	0.5	ND[b]	ND	86.3	6.1	4.1	10.2
SA4	HCl treated SA2, 6 h @100 °C	0.9	ND	ND	86.8	2.6	2.8	5.4
SA5	TEMPO treated SA2	29.6	ND	ND	34.4	2.3	ND	2.3
SA6	Red pine, Control	28.9	1.4	3.2	41.9	6.6	10.4	21.6
SA7	NaOH treated red pine holocellulose	0.8	0.6	0.9	69.1	3.2	14.4	19.1
SA8	Douglas fir, control	29.3	1.2	2.7	48.0	4.6	14.4	22.9
SA9	SPORL[c] treated Douglas fir, #3	24.6	ND	0.3	67.7	2.5	3.1	5.9
SA10	SPORL treated Douglas fir, #7	45.1	ND	0.4	53.7	0.9	1.3	2.6
SA11	Delignified SA8	6.9	1.1	2.5	56.6	5.2	15.2	24.0
SA12	Delignified SA9	6.3	ND	ND	90.1	3.0	2.7	5.7
SA13	Delignified SA10	3.0	ND	0.3	90.4	1.0	0.8	2.1
SA14	Loblolly pine control	30.7	1.5	2.4	41.3	6.2	9.7	19.8
SA15	Loblolly pine, supposedly CNC fraction[d]	38.1	0.1	0.2	30.0	0.7	1.0	2.0
SA16	Loblolly pine, membrane filtered fraction[e]	75.8	0.1	0.2	13.8	0.6	0.6	1.5
SA17	BNSWKP[f]	0.5	0.3	ND	81.3	7.5	5.2	14.0

[a] Hemicellulose is sum of xylan, mannan, arabinan, and galactan. Because the pine and fir samples have glucomannan, in these, part of the glucose is hemicellulose as well

[b] Not detected

[c] Sulfite pretreatment to overcome recalcitrance of lignocellulose

[d] Supposedly CNC fraction, had higher glucan content compared to SA16

[e] High lignin fraction that passed through the membrane filter

[f] Bleached northern softwood kraft pulp

water as possible with a pipette. Approximately 10 ml of 4 M HCl was added and the mixture set to stir. After 8 h a portion was removed and neutralized with dilute NaOH to pH 7. The material was centrifuged and isolated (Table 1, SA3). Another portion of SA2-ND, after removing excess water, was placed in a 25 ml Erlenmeyer flask. 20 ml of 4 M HCl was added along with a stir bar. A cover plate was placed on the flask and the flask placed in a 100 °C PEG bath for 6 h. The solution had a slight yellow cast. The material was filtered on a sintered glass funnel and copiously washed until the filtrate had a pH of 6 (Table 1, sample ID SA4).

For TEMPO treatment of SA2-ND the method used is based on reference (Saito et al. 2007 and personal communications with Dr. Akira Isogai). First, water content of the wet sample was determined. For this, an aliquot of SA2-ND (~44.3 mg wet) was allowed to air dry and sample weight was obtained (5.7 mg). A wet amount of SA2-ND equivalent to 250 mg air-dried was placed in a 50 ml Erlenmeyer flask along with 25 ml of water, 4 mg TEMPO and 25 mg sodium bromide. 1.25 g of 14.8 % NaClO was adjusted to pH 10 with 0.1 M HCl. and was added on a 10 mM NaClO to 1 g of sample basis. The mixture was stirred at RT. 0.5 M NaOH was added to keep the pH near 10 until the pH was stabilized. This sample is designated as SA5 in Table 1.

SPORL treated Douglas fir samples

Two samples of Douglas fir that were treated with the published SPORL (sulfite pretreatment to overcome recalcitrance of lignocellulose) process (Leu et al. 2013) were obtained from Dr. J. Y. Zhu at FPL. The samples (Table 1, SA9 and SA10) were selected for their low amount of hemicellulose and differing amounts of lignin. These samples and the Douglas fir control were delignified (Table 1; SA11, SA12, and SA13) using acid chlorite as outlined earlier (Agarwal

Table 2 Raman spectral changes upon sampling in D_2O

Sample ID	Sample description	Bands showing intensity change[a], 1550–250 cm^{-1} H_2O versus D_2O							Bands showing frequency shift[b], 1550–250 cm^{-1} H_2O versus D_2O				
SA2-ND[c]	NaOH treated aspen wood holocellulose,	1380 ↑ 75.6 ± 6.5 %	1323 ↑	1295 ↑	1120 ↑	997 ↑	970 ↓	897 ↓	1418 → 1420	1338 → 1346	1149 → 1153	1121 → 1123	996 → 999
SA4-ND	SA4, HCl treated SA2; HCl, 6 h @100C;	1380 ↑ 36.4 ± 0.8 %	1323 ↑	1295 ↑	1120 ↓	997 ↑	970 ↓	897 ↓	1419 → 1422	1338 → 1347	1151 → 1153	1121 → 1123	996 → 999
SA7-ND	NaOH treated red pine holocellulose,	1380 ↑ 70.1 ± 2.9 %	1323 ↑	1295 ↑	1120 ↑	997 ↑	970 ↓	897 ↓	1412 → 1424	1340 → 1346	1149 → 1152	1121 → 1123	997 → 999
SA13	Delignified SPORL[d] treated Douglas fir, #7	1380 ↑ 46.2 %	1323 ↑	1295 ↑	1120 ↑	997 ↑	970 ↓	897 ↓	1418 → 1420	1338 → 1346	1149 → 1153	1119 → 1122	996 → 999
SA17	BNSWKP	1380 ↑ 39.3 ± 2 %	1323 ↑	1295 ↑	1176 ↑	997 ↑	970 ↓	899 ↓	1420 → 1421	1338 → 1342	1151 → 1153	1121 → 1123	997 → 999
SA18	Tunicate cellulose	1380 ↓ 1.51 ± 9.6 %	–	–	–	–	–	–	–	–	–	–	–
SA19	Amorphous cellulose	1380 ↑ 154.3 ± 1.5 %	–	1295 ↑	1175 ↑	997 ↑	1005 ↑	899 ↓	1414 → 1419	1339 → 1350	1145 → 1175	1118 → 1124	995 → 1005
SA20	Pulp-CNCs	1380 ↑ 38.9 ± 4.0 %	1339 ↓	1293 ↑	1179 ↑	997 ↑	970 ↓	899 ↓	1420 → 1422	1339 → 1347	1149 → 1153	1121 → 1123	997 → 999
SA21	Avicel	1380 ↑ 37.7 ± 1.4 %	1323 ↑	1295 ↑	1176 ↑	997 ↑	970 ↓	899 ↓	1420 → 1421	1338 → 1340	1151 → 1153	1121 → 1123	997 → 999
SA22	Whatman CC-31	1380 ↑ 19.0 ± 1 %	1338 ↓	1295 ↑	1176 ↑	997 ↑	970 ↓	899 ↓	–	–	1152 → 1153	1121 → 1122	996 → 997
SA24	*Cladophora* cellulose	1380 ↓ 1.01 ± 1.2 %	–	–	–	–	–	–	–	–	–	–	–
SA26	Cellulose II; CC31	1380 ↑ 145 ± 4.0 %	NA[e]	1295 ↑	1177 ↑	997 ↑	1005 ↑	899 ↓	1414 → 1417	1338 → 1348	NA	1098 → 1100	996 → 1008
SA27	Avicel + 10 % xylan	1380 ↑ 37.8 ± 4.0 %	1339 ↓	1295 ↑	1175 ↑	997 ↑	NA	899 ↓	1421 → 1423	1338 → 1341	NA	1121 → 1123	997 → 998

Table 2 continued

Sample ID	Sample description	Bands showing intensity change[a], 1550–250 cm^{-1} H_2O versus D_2O					Bands showing frequency shift[b], 1550–250 cm^{-1} H_2O versus D_2O			
SA28	Pulp-CNFs	1380 ↑	1320 ↑	–	1177 ↑	997 ↑	NA	–	1408 → 1410	1339 → 1341	NA	1121 → 1122	–
		33.6 ± 4.4 %											

[a] Increase (↑), decrease (↓), and no change (–) compared to intensity in H_2O

[b] (→) means "shifts to"

[c] Never dried

[d] Sulfite pretreatment to overcome recalcitrance of lignocellulose

[e] Not applicable

et al. 2013b). Lignin removal was necessary prior to Raman analysis because the samples were dark and the lignin chromophores cause high levels of fluorescence in Raman spectroscopy (Agarwal et al. 2013a).

CNC production from loblolly pine

The method used to produce CNCs from unmodified wood was similar to the one used for CNC production from bleached kraft pulp (Reiner and Rudie 2013). Air-dried loblolly pine wood (31.5 g of 40-mesh meal) was added to a three-neck, round-bottom flask equipped with a mechanical mixer, addition funnel and barbed stopcock. The flask was flushed with N_2, evacuated (3 mmHg), filled with N_2, and evacuated (3 mmHg). Next, 250 ml 64 % H_2SO_4 (room temp) were added over 1 min. The wood mass quickly turned very dark, initially appearing as a paste but the viscosity dropped in about 15 min. The acid hydrolysis reaction was carried out for 90 min at 45 °C. The contents were diluted to 4300 ml and the solids-containing portion settled to approximately 1 l. The solution was decanted then diluted to about 2.5 l. The suspension was neutralized with NaOH solution (~800 ml at 5 wt%) followed by dilution to 4300 ml. The suspension was allowed to settle overnight. Solids settled to approximately 1 l. The solution was decanted and the suspended solids dialyzed against RO (reverse osmosis) water for 1 week with daily flipping of the dialysis tubes to periodically mix the significant amount of dark solids that settle to the bottom relatively quickly. The dialyzed suspension (1.4 l) was treated with an ultrasonic probe (20 k Hz) for 12 min (100,000 J). The suspension was then centrifuged for 15 min at 10,000×*g* and decanted (this corresponds to the wood CNC suspension shown on the right in Fig. 1i). The solids were washed once by suspending again to 1 l and centrifuging at 10,000×*g* for 15 min. This decant was combined with the previous one and the total concentrated to about 20 ml using a rotovap and then dried under vacuum over P_2O_5 to yield 0.58 g solids (sugar and lignin analysis are shown in Table 1, referred as sample SA15; ~1.4 % glucan-yield based on 40 % cellulose in the wood sample). The dark solids retained by the centrifugation were air-dried to 11.7 g (sugar and lignin analysis are shown in Table 1, referred as sample SA16; ~12.8 % glucan-yield based on 40 % cellulose on wood).

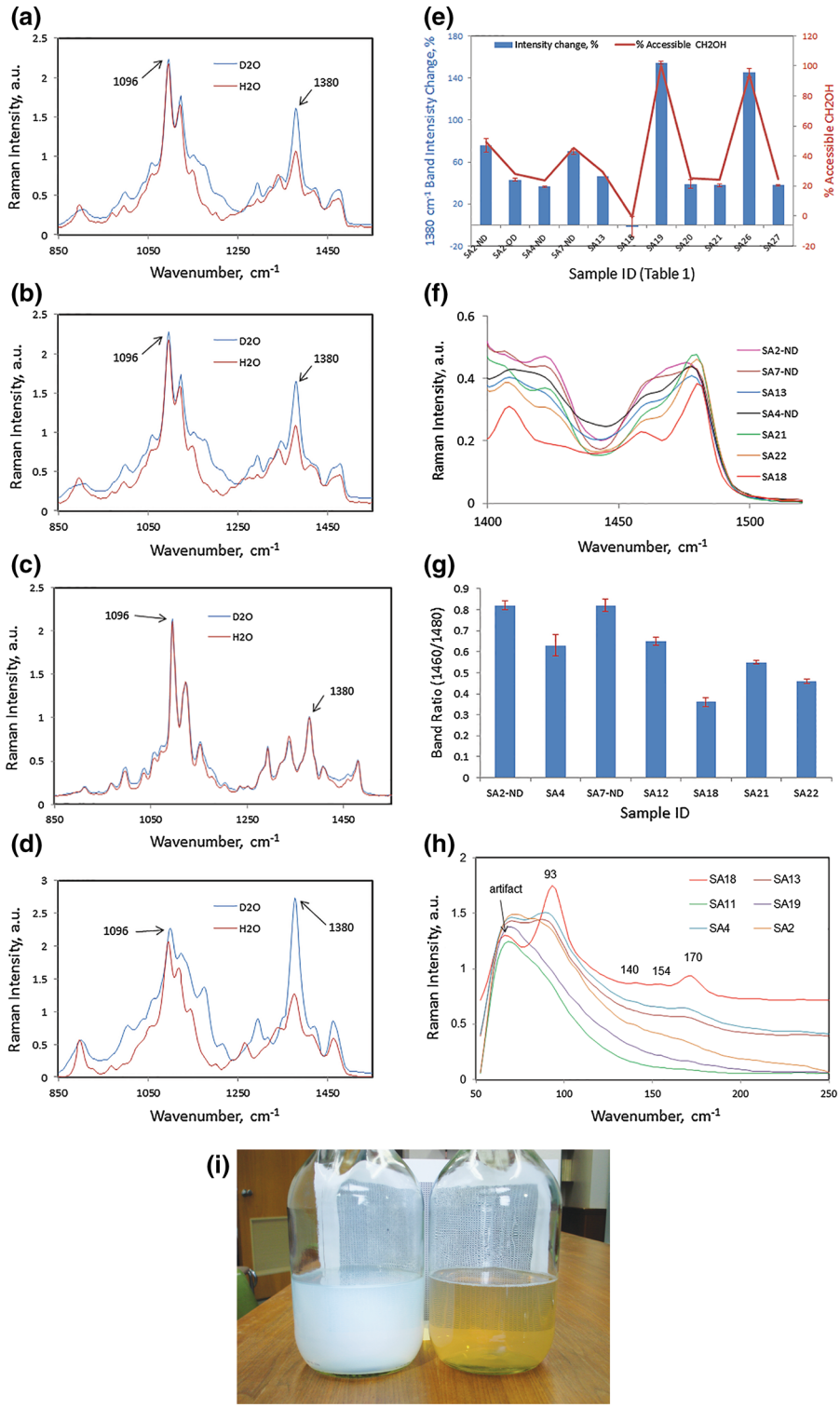

Fig. 1 Raman spectra, band intensity ratios, and images of suspended CNCs. **a–d** Raman spectra, in the region 850–1550 cm^{-1}, showing intensity enhancement of 1380 cm^{-1} band in D_2O for SA2-ND, SA7-ND, tunicate, and amorphous cellulose, respectively. **e** % change in 1380 cm^{-1} band intensity and % accessible CH_2OH for various samples. **f** Raman spectra, in the region 1400–1550 cm^{-1}, showing the CH_2 scissor mode for the CH_2OH rotamers. **g** Intensity ratio (1460/1480) representing (*gt*/*tg*) ratio in cellulose I samples. **h** Raman spectra in low frequency region (50–250 cm^{-1}. **i** Pulp CNCs (*left*) and supposedly wood CNCs (*right*). *Error bars* in (**e**) and (**g**) represent standard deviation

CNC production from bleached kraft pulp

Pulp CNCs (Table 2, SA20) were produced from commercial softwood dissolving-pulp using FPL's CNC production facility (Reiner and Rudie 2013). The process uses 64 % sulfuric acid at 45 °C. More details of the process can be found elsewhere (Reiner and Rudie 2013).

Cellulose II production from Whatman CC-31

Cellulose II used in this work (Table 2, SA26) was made from Whatman CC-31 and was produced using the procedure similar to one by Hirota et al. (2010). Whatman CC-31 cellulose was mercerized using 20 % NaOH for 1 day, filtered, rinsed with water/EtOH, treated with dil. HCl to pH 4–5, and rinsed with water/EtOH. The mercerized sample was air dried and vacuum dried at 40 °C. The Raman spectrum and XRD pattern of the mercerized cellulose confirmed that high-crystallinity cellulose II was produced.

Production of pulp-CNFs using commercial, bleached, eucalyptus kraft pulp

The dry lap pulp was pretreated overnight at room temperature by mixing at 2 % solids, pH 2 with 2 wt% $NaClO_2$ on pulp; followed by filtering and washing. Pretreated pulp (1.25 kg, OD) was added to 350 l sodium carbonate (0.6 kg) and stirred for an hour at room temperature. Sodium bicarbonate (0.1 kg), sodium bromide (0.12 kg) and TEMPO (20 g) were added and the reaction was heated to 30 °C. NaClO solution (6.2 l, 8 wt%, 5 mol/kg) was diluted to 20 l and added. The reaction was stirred overnight at 30 °C; the treated pulp was filtered and washed. Pulp yield was typically about 93 %. The carboxylated pulp is suspended at 4 % solids and processed once using a MiniDeBee homogenizer (Bee International, South Easton, MA, USA) equipped with a 125-μm orifice at 140 MPa, then diluted to 1 % solids and passed twice through the MiniDeBee homogenizer equipped with a 100-μm orifice at 175 MPa. The carboxalate content of the oxidized pulp was determined to be 1.3 mmol/g by alkali titration of the acid form of the pulp.

Chemical composition

Seventeen samples listed in Table 1 were analyzed for chemical composition. The amount of both Klason lignin (TAPPI test method 1983) and carbohydrates (arabinan, galactan, glucan, xylan, and mannan (Davis 1998) were determined. Reproducibility for Klason lignin was 0.4 %, and for the carbohydrate analysis, the standard deviation was <1 % (Davis 1998).

Recording Raman spectra, band intensity calculation, and estimating Raman crystallinity

Cellulose, pulp, wood, and treated wood samples were analyzed with a Bruker MultiRam spectrometer (Bruker Instruments Inc., Billerica, Massachusetts). This Raman system is equipped with a 1064-nm 1000-mW continuous wave (CW) diode pumped Nd:YAG laser. Samples were prepared in two ways for analysis—either by making a pellet in a pellet press or by sampling in shortened NMR glass tubes. Some samples were sampled in both ways. Numerous samples were analyzed in presence of H_2O and D_2O in addition to analyzing them in the dry state in the tube. This was done to study the effect of OH to OD exchange. For Raman crystallinity estimation purposes (Agarwal et al. 2010, 2013a), spectra were obtained from pellets of $\sim$0.1 g. The laser power used for sample excitation was 900 mW but in cases where significant fluorescence was encountered or the possibility of thermal degradation existed, the power was reduced to 600 mW. Depending upon the S/N desired and the concentration of the sample (in H_2O or D_2O) anywhere from 1024 to 16,384 scans were co-added. Some samples (e.g., CNCs and CNFs in H_2O or D_2O) were quite dilute and to get better S/N ratio 16,384 scans were obtained. OH to OD exchange was performed by removing excess water, putting the sample in D_2O (99.9 % deuterated), then centrifuging ($4000\times g$) the sample in NMR tube, and removing excess D_2O. Thereafter, this process was repeated in the sampling tube itself one more time and a Raman spectrum was obtained to determine how the OH and OD regions compared. This spectrum was also compared with the Raman spectrum of the sample in the dried state to evaluate how much H_2O was still present. In most cases a third D_2O exchange was not needed but in cases where needed another iteration of replacing old with new D_2O was carried out. Spectra were also obtained from samples that were dried in different ways, dried at room temperature (RT), by freeze drying, and in an oven at 110 °C. OPUS 7.2 software was used to find peak positions and process the spectral data.

For experiments that have to do with Fig. SI2, where it is shown that OH to OD exchange leads to intensity increase at 1380 cm^{-1}, the RT dried samples were immersed in D_2O prior to freeze drying or oven drying. However, it needs to be noted that during such experiments no attempt was made to completely exchange the available OH groups with the OD groups. Moreover, all samples were analyzed in the pellet form and post freeze drying (or oven drying), no precaution was taken to avoid the exchange of the sample's OD groups with atmospheric moisture.

Processing of spectra involved normalization, various mathematical operations, and background removal. Background correction was performed using the "rubberband option" in OPUS and 64 baseline points. The method is based on the polynomial fitting of the background. For plotting purposes, the spectra were converted to ASCII format which then allowed the spectral data to be imported to Excel. Details of band intensity calculation and crystallinity determination by Raman are provided in Agarwal et al. (2010). Using OPUS, intensities (peak heights) of the 1380 and 1096 cm^{-1} bands were calculated by a "one baseline point method" that involved choosing a minimum intensity wavenumber near the peak (e.g., 1440 and 950 cm^{-1} for 1380 and 1096 cm^{-1} bands, respectively) and drawing a horizontal line (from that wavenumber) under each peak. Subsequently, the peak heights were measured from this horizontal line. However, for the 1480 and 1460 cm^{-1} bands, the "two baseline points" method was selected and two baseline points were 1441 and 1500 cm^{-1}. A sloping baseline was drawn between these points and peak heights at 1460 and 1480 cm^{-1} were measured from the baseline. The intensity data were exported to Excel, where Raman band intensity ratios were calculated.

Using the previously established correlations (Agarwal et al. 2010, 2013a) that were based on the Bruker RFS-100 and MultiRam instruments, the univariate Raman crystallinities (X) were estimated. Based on RFS-100, Eq. (1) was developed for estimating the Raman crystallinity (Agarwal et al. 2010) and because MultiRam was used in the present investigation, the inter-instrument calibration correction (RFS100 vs. MultiRam) was carried out using Eq. (2) to get the RFS-100 equivalent crystallinity (XRFS-100).

$$X_{MultiRam} = ((I_{380}/I_{1096}) - 0.0286)/0.0065 \quad (1)$$

$$X_{RFS-100} = (X_{MultiRam} + 2.0212)/0.8222 \quad (2)$$

Additionally, the spectra were corrected for change in the response of the MultiRam optics over time. Using the white light in the sample compartment, the "reference correction" was performed on each sample spectrum. Where necessary, the estimated Raman crystallinities are also corrected for the hemicellulose contributions (Agarwal et al. 2013a). Of the samples listed in Table 3, syringyl-lignin correction was required (Agarwal et al. 2013a) only for SA1 (Table 3) because in the case of others, either only guaiacyl lignin was present or lignin has been mostly removed.

Considering that the Raman features of cellulose and hemicellulose are similar and overlap (Agarwal and Ralph 1997), one of the challenges for our Raman experiments was to remove most of lignin and hemicellulose without modifying cellulose. For these purposes, the approach used was delignification of wood at room temperature (25 °C) followed by extended-NaOH-extraction at room temperature (Atalla et al. 2014). As expected, compared to control aspen and red pine wood samples (Table 1, SA1 and SA6, respectively) the samples treated with the above mentioned procedure (Table 1, SA2 and SA7, respectively), contained significantly reduced amounts of Klason lignin and xylan (Table 1). For the aspen-derived sample (SA2), additional reduction of xylan was achieved when the NaOH-treated aspen-holocellulose sample was further treated with HCl (SA3 and SA4, Table 1) or was subjected to TEMPO (2,2,6,6-tetramethyl-1-piperidinyloxy) treatment (SA5; Okita et al. 2010; Saito et al. 2007). Compared to SA2, SA4 and SA5 had significantly lower amounts of xylan (Table 1; 6.6, 2.6, and 2.3 %, respectively for SA2, SA4, and SA5). Similarly, compared to SA2, in SA4 and SA5, mannan content also declined (Table 1; 3.5, 2.8, and ~0 %, respectively for SA2, SA4, and SA5). Although the least amounts of xylan and mannan were present in sample SA5 considering the possibility that the treatments can modify the aggregated state of aspen wood cellulose (Atalla et al. 2014; Langan et al. 2014; Nishiyama et al. 2014) a number of samples were analyzed in Raman.

X-ray diffraction and Segal-WAXS crystallinity calculation

Wide-angle X-ray diffraction profiles were recorded in the reflection mode on a Bruker D8 Discover diffractometer

Table 3 Comparison of intensity ratio (1460/1480) in various samples of cellulose

Sample ID	Sample description	Ratio (1460/1480)	Ratio higher compared to tunicate, %
SA2-ND	NaOH treated aspen wood holocellulose, never-dried, H_2O versus D_2O	0.82 ± 0.02	125.5
SA4	HCl and NaOH treated aspen wood holocellulose	0.63 ± 0.05	74.6
SA7-ND	NaOH treated Red pine wood holocellulose, never-dried, H_2O versus D_2O	0.82 ± 0.03	125.7
SA12	Delignified SPORL treated Douglas fir, #3	0.65 ± 0.02	78.8
SA18	Tunicate	0.36 ± 0.02	0
SA21	Avicel	0.55 ± 0.01	52.5
SA22	Whatman CC-31	0.46 ± 0.01	27.8
SA27	Avicel + 10 % xylan	0.60 ± 0.01	64.7

with monochromatic CuKα (λ = 1.5418 Å) point source and a VÅNTEC-500 detector at the Materials Research Science and Engineering Center, University of Wisconsin, Madison. Segal-WAXS crystallinity was calculated using the peak height method (Segal et al. 1959; Park et al. 2010). The X-ray diffractometer beam aperture of 0.5 mm was used. In all cases, diffractograms were obtained on the same samples (in the pellet form) that were previously analyzed in FT-Raman. In WAXS, both sides of a particular pellet face were sampled and average values of the parameters are reported. FWHM and peak position for the [200] reflection were determined from the diffractograms of the samples (Table 4).

For each of the samples in Table 4, Segal-WAXS crystallinity was calculated by subtracting the amorphous contribution approximately at $2\theta = 18\,^{\circ}$ ($100 \times (I_{22.5} - I_{18})/I_{22.5}$); called Segal-WAXS (Park et al. 2010). This was done after a straight line was drawn between the lowest intensity points in the 2θ range of 7 ° and 37 °. This method is similar to the [200] peak height ratio method (Park et al. 2010), although in the latter method, the background subtracted was based on a blank sample run.

Results and discussion

Raman investigations suggest never-dried microfibrils are D_2O accessible. To test the hypothesis that fibril cellulose is non-crystalline, first the effects of H_2O-to-D_2O exchange on the Raman spectra of the various cellulose samples were evaluated. The idea was that in a non-crystalline structure, deuterated water should have access to the interior of the fibrils but there would be less effect on crystalline samples. For this purpose, a number of samples whose chemical compositions are listed in Table 1 were used in the Raman experiments. The detailed compositional information was needed to interpret spectral data of various samples (see below).

On the other hand, sample SA7, a softwood holocellulose, contained a significant amount of mannan after the alkali treatment (19.1 % SA7, Table 1) and its hydrolysis using HCl did not significantly reduce the mannan content (data not reported here). Therefore, another option was explored where samples of SPORL-treated Douglas fir (SA9 and SA10, Table 1) were used because the treatment successfully removed both xylan and mannan (Table 1; xylan 2.5 and 0.9 %, respectively in SA9 and SA10; mannan 3.1 and 1.3 %, respectively in SA9 and SA10). Once again, mindful that the aggregated state of cellulose could be modified by various treatments, a number of softwood samples were analyzed by Raman spectroscopy.

Upon OH to OD exchange, all the accessible hydroxyls will be OD-exchanged including the O6s. However, considering that our measurement was based on Raman band at 1380 cm^{-1}, which represents only the CH_2OH bending modes (Wiley and Atalla 1987), the information was obtained only on the C6s. Raman spectra, in the region 850–1550 cm^{-1}, obtained in presence of water and D_2O of four types of cellulose samples (Table 2) are shown in Fig. 1

Table 4 Crystallinity (Segal-WAXS and Raman), XRD [200] peak position and FWHM of various samples

Sample ID	Sample description	Crystallinity[a], %		[200] peak position	[200] FWHM
		Segal-WAXS	Raman[b]		
SA1	Aspen wood, control	77.0	49.9[c]	22.5	3.1
SA2-RT	NaOH treated aspen holocellulose, RT	75.3	47.9	22.2	3.0
SA2-OD	NaOH treated aspen holocellulose, OD	80.1	ND[d]	22.3	2.8
SA6	Red pine, control	76.8	57.4	22.5	3.6
SA7-RT	NaOH treated red pine holocellulose, RT	75.5	56.6	22.2	3.1
SA7-OD	NaOH treated red pine holocellulose, OD	70.1	ND	22.2	3.3
SA8	Douglas fir, control	77.0	50.4	22.5	3.5
SA9	SPORL treated Douglas fir, #3	83.4	ND	22.7	2.3
SA10	SPORL treated Douglas fir, #7	80.7	ND	22.7	2.3
SA11	Delig. Douglas fir, control	79.2	60.9	22.6	2.9
SA12	Delig. SPORL treated Douglas fir, #3	88.3	ND	22.7	2.2
SA13	Delig. SPORL treated Douglas fir, #7	88.3	52.6	22.7	2.0
SA17	BNSWKP[e]	82.5	53.2	22.4	2.3
SA18	Tunicate cellulose	95.6	86.5	22.8	1.0
SA19	Amorphous cellulose	23.18	−4.4[f]	20.7	NA[g]
SA21	Avicel cellulose	87.5	59.1	22.7	2.3
SA22	Whatman CC-31	93.5	82.2	22.7	1.4
SA23	Bacterial cellulose	92.0	65.6	22.7	1.3
SA24	*Cladophora* cellulose	95.7	82.5	22.9	0.7

[a] In the context of the present investigation, for wood and wood-derived samples, FWHM (XRD) can be considered as "degree of lateral order" or DOLO. Note that in XRD, FWHM is related to crystallinity (Fig. 4)

[b] Where needed, Raman values are corrected for hemicellulose contribution

[c] From Agarwal et al. (2013a)

[d] Not done

[e] Bleached northern softwood kraft pulp

[f] From Agarwal et al. (2010)

[g] Not applicable

(Fig. 1a–d). The spectra of aspen cellulose in the never dried (ND) state (Table 2, SA2-ND), red pine cellulose in the never dried state (Table 2, SA7-ND), tunicate cellulose (Table 2, SA18), and amorphous celluloses (Table 2, SA19) are shown in Fig. 1a–d, respectively. In the expanded form and with some of the specific bands annotated, the spectra are also shown in Fig. SI1. Each sub-figure consists of 2-spectra—one obtained in water and the other in D_2O. The two spectra in the set were normalized on the 1096 cm^{-1} band of cellulose. In the case of wood and amorphous samples, several spectral changes were observed upon D_2O immersion. The most prominent changes are summarized in Table 2. These changes consisted of band intensity changes (up and down arrows represent increase and decrease in intensity, respectively) as well as band frequency shifts (indicated by a horizontal arrow meaning "shifts to"). The spectral changes arise from the exchanges of cellulose OH with OD groups (Figs. SI1 and SI2).

For wood celluloses (Table 2; Fig. SI1), upon D_2O immersion, one of the most informative spectral changes was the intensity increase of the 1380 cm^{-1} band (Fig. 1; Table 2; the 1380 cm^{-1} peak is representative of CH_2 twisting mode). However, to show that indeed 1380 cm^{-1} intensity increases upon OH-to-OD exchange, various cellulose samples were deuterated by either freeze drying or oven drying from D_2O and area-intensity of OD stretch region and peak-height intensity change at 1380 cm^{-1} were measured and are shown in Fig. SI2. This Figure clearly shows that, for each of the dried (from

D_2O) samples, presence of OD groups resulted in an intensity increase at 1380 cm^{-1}. It is noteworthy that during such experiments no attempt was made to completely exchange the available OH groups with the OD groups. Therefore, not only are the results not comparable among the samples, but, generally speaking, these data on changed intensity at 1380 cm^{-1} will be same or lower when compared with such data from never-dried samples that were fully exchanged. In both the regions, (OD stretch and 1380 cm^{-1} intensity change), the highest values were obtained for amorphous cellulose (SA19-freeze dried). This is expected because amorphous cellulose when analyzed in D_2O had earlier produced 154 % intensity enhancement at 1380 cm^{-1} (Table 2, SA19).

Changes in the 1380 cm^{-1} band intensity were compared between wood, amorphous, tunicate, and other celluloses (Table 2; Fig. 1e). Whereas, on one hand, in the case of amorphous cellulose (Fig. 1d, e) the peak intensity increased by 154 %, in contrast, no intensity change occurred for tunicate cellulose (Table 2, SA 18; a decline of 1.5 % is within the experimental error). Moreover, wood cellulose that was mostly in its never-dried, native state (present in treated woods SA2-ND and SA7-ND), showed intermediate change (Table 2, ~70 to 75 % increase). The role of the presence of small amounts of xylan (in SA2-ND) and glucomannan (in SA7-ND) has been investigated and it was concluded that their presence did not make significant change to the % increase of the 1380 cm^{-1} band intensity (e.g., for xylan, Table 2, SA21 vs. SA27). Therefore, the intensity increase is mostly due to cellulose and attributable to OH to OD exchange on the hydroxymethyl groups (Fig. SI2). Additionally, although harsher thermochemical treatments further reduced the content of hemicellulose (Table 1; SA4, SA5, SA12, and SA13), the treatments resulted in reduced 1380 cm^{-1} band intensity change (Table 2, only data for SA4 and SA13 is provided). Moreover, the LF Raman bands in Fig. 1h started to appear in SA4 and SA13. These changes implied that cellulose structure was being consolidated—an observation previously reported by researchers in different investigations (Kafle et al. 2015; Atalla et al. 2014; Langan et al. 2014; Xu et al. 2013; Driemeier et al., 2011; Hult et al. 2003; Liitia et al. 2003). This is evident from the data in Table 2 and Fig. 1e where the intensity increase upon OD exchange declines for SA4 and SA13 compared to SA2-ND and SA7-ND. The structure consolidation means that compared to the never-dried native state accessibility of D_2O to cellulose chains is limited. For various samples, Fig. 1e also shows % CH_2OH groups that were accessible to D_2O (second y-axis). This is based on the assumption that in amorphous cellulose all the CH_2OH groups are fully accessible to the OD exchange and hence, all of the CH_2OH groups are deuterated.

To explain the observed "% accessible CH_2OHs" in the native fibrils of SA2-ND and SA7-ND (Fig. 1e), a number of cellulose crystalline models were considered (Table SI1). These models were similar to the ones described in the publications of Elazzouzi-Hafraoui et al. (2008), Sèbe et al. (2012), and Fernandes et al. (2011). Height and width of various diffraction intensities as well as the number of surface chains are dependent upon both size and shape of the crystal. One such 36 chain model (6 × 6) is shown in Fig. SI3. Considering that microfibril models with 18- to 36-chains of cellulose have been proposed/discussed (Kuramae et al. 2014; Jarvis 2013; Newman et al. 2013; Fernandes et al. 2011, Newman 2008), we decided to compare the ability of the models to explain the Raman based cellulose accessibility data. The analysis of 36-chain and other models (Table SI1) showed that based on the number of chains available on the crystallite surface, the O6 accessibility was in the range of 28–39 % (Table SI1). This was significantly lower than what was found experimentally (50 %, Fig. 1e). Nevertheless, irrespective of the number of chains in a microfibril, a model with disordered chains can explain the 1380 cm^{-1} band based Raman observations. In this analysis of the models, every other surface O6 was considered to be unavailable for exchange due to its facing towards the interior, and no independent amorphous content was considered. In native wood, the existence of serial amorphous regions independent of the microfibrils is not supported by the TEM images where no such regions have been detected (Kuramae et al. 2014, Saito et al. 2007).

Further evidence that the CH_2OH exchanges were occurring in the interior regions came from the Raman investigation of the pulp cellulose nano-fibrils (CNFs). In the case of this sample (Table 2, SA28) where the COOH level was 1.3 mmol/g, all of the surface CH_2OH groups were considered to have been carboxylated (Okita et al. 2010). Nevertheless, the

intensity of the 1380 cm^{-1} band still increased by 33.6 % upon sampling in D_2O (Table 2, SA28). Moreover, in the case of tunicate cellulose, which is highly crystalline and consequently showed no 1380 cm^{-1} band intensity sensitivity (Table 2, SA18), deuteration of surface CH_2OH groups had no influence on the spectrum in D_2O (Fig. 1c). This may point to Raman's reduced sensitivity to surface CH_2OH groups. For tunicate cellulose, because its crystal size is large, a rough analysis showed that there should to be about 18 % CH_2OH groups on the surface. But regardless, no change in 1380 cm^{-1} band intensity occurred.

When the spectra of tunicate, amorphous, and aspen- and pine-wood (Table 2; SA18, SA19, and SA2-ND and SA7-ND, respectively; Fig. SI1) were obtained in D_2O and in H_2O were compared, none of the Raman peaks showed any shift for highly crystalline tunicate cellulose. This is likely to be due to inaccessibility of tunicate's interior OH groups to D_2O. In contrast, many bands of amorphous cellulose showed significant shifts (Table 2, SA19; Fig. SI1). That indicated most cellulose OH groups were exchanged to OD and the varying band shifts were likely to reflect the extent to which the vibrational modes had contributions from the OH/OD groups (Wiley and Atalla 1987). Such shifts of vibrational modes have also been reported in the IR spectra of deuterated bacterial cellulose (Bali et al. 2013). Spectral shifts of wood-celluloses (Table 2, SA2-ND and SA7-ND) were found to be lower than the values obtained for amorphous cellulose (SA19, Table 2) and therefore, indicated that the OHs in wood celluloses were not all freely accessible to D_2O. For example, the shift seen for the 1118 cm^{-1} band of amorphous cellulose (Table 2, SA19) indicated that the mode represented by this band experiences some influence from OH groups and when all OHs are replaced by ODs the band frequency increased by 6 cm^{-1} to 1124 cm^{-1}. However, for the wood celluloses (SA2-ND and SA7-ND) the shift is limited to 2 cm^{-1} (Table 2, 1121 to 1123 cm^{-1}). This implies that not all OHs were exchanged with ODs. Similar behavior was shown by some additional bands where contributions of the O–H groups were present. In the case of wood cellulose, which experienced limited changes compared to the changes in amorphous-cellulose, the latter implied that such OH to OD exchange was incomplete and consequently, some D_2O-inaccessible domains remained in the structure of never-dried native cellulose. Nevertheless, a large part of cellulose structure was accessible to D_2O. Taken together with the band intensity changes, the Raman shift changes were indications of cellulose-D_2O interactions at the molecular level and, based on our 36-chain models, indicate that interior cellulose OH groups were partly replaced by cellulose OD groups.

Presence of various CH_2OH rotamers

Another important piece of information was found from the Raman contributions of the CH_2 scissor mode (1450–1500 cm^{-1}) in cellulose. In most samples of cellulose I, two bands can be clearly seen although a third may also be present (Fig. 1f). The two contributions, present at approximately 1460 and 1480 cm^{-1}, represent the scissor mode of *gt* and *tg* conformations of the hydroxy methyl group (Fig. 2), respectively (Table 3; Horii et al. 1983; Chen et al. 2015). A third band representing the *gg* rotamer (Fig. 2) may also exist between these two band positions, but remained unresolved in the present study. The intensity ratio (1460/1480) is reported in Table 3 and shown as a bar chart in Fig. 1g. Further, in the case of pure cellulose I samples, the band intensities ratio (1460/1480) and non-crystallinity had been shown to be linearly correlated (Schenzel et al. 2005). The reported finding is also supported by the data in Table 4 where Segal-WAXS and Raman crystallinities of a number of cellulose samples are listed. Compared to tunicate (Table 3, SA18), where the ratio had a low value due to tunicate's high crystallinity, wood-celluloses (Fig. 1g, Table 3; SA2-ND, SA4, SA7-ND, and

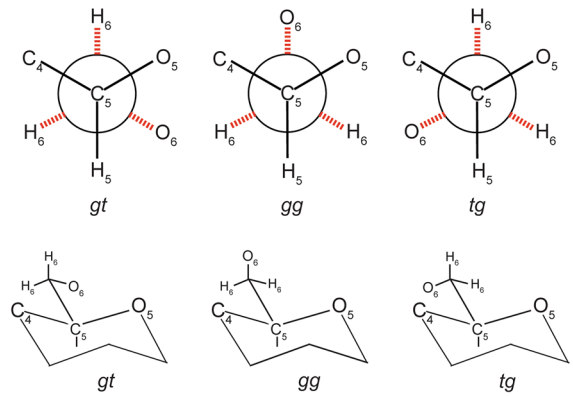

Fig. 2 *gt*, *gg*, and *tg* conformers of CH_2OH groups

SA12) presented a significantly higher ratio (75–125 % higher, Table 3; Fig. 1g) and therefore, low crystallinity. Although, to describe the degree of order in cellulose, until now we have used the traditional terminology of "crystallinity", however, in the context of the present investigation, a more appropriate phrase would be "degree of lateral order" or DOLO for short. In wood celluloses (SA2-ND, SA4, SA7-ND, and SA12; SA4 and SA12 were air dried samples) the increased intensity at 1460 cm^{-1} implies increased number of CH_2OH rotamers with *gt* conformation. This in turn has important consequence for the formation of inter-chain H-bonds because the chain-locations with the local *gt* CH_2OH conformation would be unable to form in plane (intra-sheet) H-bonds with the neighboring chains. This implies lack of lateral order at the nano scale within the structure of cellulose. Therefore, the existence of multi-rotamers of CH_2OH seems to be the primary reason behind the non-crystallinity of the fibrils. Nevertheless, in the cell wall microfibrils, the regions with *tg* CH_2OH conformations are also present implying that regions with and without the interchain H-bonds coexist within the same microfibril. Consequently, it is likely that the OH to OD exchange takes place where the interchain H-bonds are absent.

Low frequency (LF) Raman modes indicate non-crystalline nature of microfibrils

Only recently were LF (< 250 cm^{-1}) Raman bands of cellulose materials reported (Agarwal 2014). Agarwal reported bands of a number of cellulose I crystalline materials along with that of amorphous cellulose and polymorphs of Avicel. All the crystalline materials had good intensity peaks. In Fig. 1h, spectra of a number of cellulose/treated-woods/wood-celluloses are compared in the LF region (50–250 cm^{-1}). Clear contributions were detected from highly crystalline tunicate cellulose (SA18) at 93, 140, 154, and 170 cm^{-1}. Similar bands have also been reported previously for Avicel (SA21) and *Valonia* and tunicate (SA18) celluloses (Agarwal 2014). Here, in Fig. SI4, the LF Raman spectra of bleached kraft pulp (SA17), Avicel (SA21), and Whatman CC-31 (SA22) are compared with those of highly crystalline celluloses (tunicate—SA18 and *Valonia*). In contrast, no signal at these positions was detected for alkali-treated aspen wood holocellulose (SA2), delignified Douglas fir (SA11), and amorphous cellulose (SA19, Tables 1, 4; Fig. 1h). However, for the alkali-treated holocellulose sample of aspen wood that was boiled for 6 h in 4 N HCl (SA4) and delignified SPORL-treated Douglas fir (SA13) there were weak contributions at 86 and 170 cm^{-1} (Fig. 1h). These contributions are likely to have come about due to the formation of new hydrogen bonds between cellulose molecules instead of between cellulose and water. And in case of wood cellulose, this can be considered as the beginning of crystal formation because the H-bonds formed upon severe thermochemical treatments (Table 1). LF contributions in cellulose are plausibly from phonon modes of the crystals and/or H-bonds (Colaianni et al. 1995; Parrott et al. 2009). Indeed, based on the interaction of Terahertz (THz) radiation with optical phonons in crystal lattices, Vieira and Pasquini (2014) reported last year that in the case of microcrystalline cellulose a band at ~3 THz (corresponds to 99.9 cm^{-1}) was present. This is in line with the Raman bands reported at 93 cm^{-1} in Fig. 1h and SI4 for tunicate cellulose (SA18), Whatman CC-31 (SA22), and bleached kraft pulp (SA17). No bands due to amorphous cellulose were seen in the THz spectra. Similarly, in the case of native state microfibrils, lack of bands in LF Raman region further showed the non-crystalline nature of the fibrils. The absence of LF Raman bands in the microfibrils supports non-crystalline nature of the fibrils irrespective of the number of chains in a microfibril. From the Raman's point of view, a microfibril could have 18 or 36 chains; either would be non-crystalline. Therefore, only an 18-chain model that is non-crystalline qualifies, not one that is crystalline at the core.

To emphasize the fact that such LF Raman vibrations are indeed due to both lattice and H-bond vibrations readers are referred to LF Raman investigation of benzoic acid single crystals where 13 bands were detected (Colombo and Furic 1971). The authors reported that the LF region contained bands due to both lattice and H-bond vibrations.

Wood cell walls failed to produce CNCs

It was reasoned that if indeed the never-dried cellulose fibrils were noncrystalline then the production of CNCs from wood would not be feasible. To test this hypothesis, loblolly pine (SA14) wood meal was acid hydrolyzed using H_2SO_4 under experimental

conditions typically used for generation of CNCs from wood-pulps (Reiner and Rudie 2013). Indeed, as shown in Fig. 1i, no CNCs were obtained. Compared to the bottle containing the pulp CNC suspension (Fig. 1i, left image) the supposedly wood CNCs containing bottle suspension (Fig. 1i, right image) was mostly transparent. This further supported the non-crystalline nature of the fibrils. The compositional analysis of the filtration membrane-retained and membrane-filtered fractions (Table 1, SA15, SA16 are retained and filtered portions, respectively) yielded no significant concentration of CNCs, indicating that these cellulose fibrils failed to generate CNCs. Although 30 % glucan was present in the membrane-retained fraction (SA15; The glucan amount was only $\sim$1.4 % of the cellulose content in wood). However, further analysis by XRD and IR showed it not to be CNCs. Moreover, to address the possibility of the presence of lignin (in wood) being detrimental to the production of the CNCs, the experiment was repeated with delignified wood meal (SA14) but the outcome remained similar. This indicated that lignin did not hinder the generation of the CNCs from cell wall microfibrils.

To understand the above result and further considering that CNCs were produced from the wood-pulp (SA17), the role of thermal treatment on wood fibrils was studied. Remarkably, CNCs were produced from the same wood meal after it was heated to 170 °C in water and subsequently acid hydrolyzed under identical conditions. This suggested that the thermal treatment was responsible for the hornification/crystallization of the microfibrils in wood.

Interpretation of X-ray data

Typical WAXS diffractograms of various samples (Table 4; SA7-RT, SA7-OD, SA6, SA17, SA18, SA19) are shown in Fig. 3. Compared to the narrow peaks in the diffractogram of tunicate (e.g., for [200] peak FWHM (full width at half maximum) = 1.0 °, Table 4 and Fig. SI5), significantly broader peaks were obtained in the case of wood and wood-derived samples ([200] FWHM varies from 2.0 ° to 3.6 °, Table 4 and Fig. SI5). Moreover, compared to tunicate cellulose, for the control and variously treated wood samples the [200] peak position was at lower 2θ (Table 4; Fig. SI6). Traditionally, both these observations have been explained in terms of contributions of crystallite size, hemicellulose, lignin, or amorphous cellulose. However, in light of our findings above, we have entertained the idea that the cellulose molecules are present, on average, in aligned but in a non-crystalline state that is responsible for these observations ([200] peak position and FWHM). Upon removal of the lateral disorder and consolidation of the cellulose chains, the diffractogram would become sharper and hence, become more comparable to that of tunicate cellulose—which we agree is highly crystalline.

The previous comments imply that there ought to be a relationship between increased DOLO (lower FWHM) and crystallinity. The plot in Fig. 4 bears this out where Segal-crystallinity was found to be linearly correlated with FWHM (Fig. 4, $R^2 = 0.89$). However, a less than perfect relationship may have to do with the fact that in different samples different types of disorder may be present. Our interpretation gets further support from a study that provided calculated WAXS diffractograms for a set of fiber models

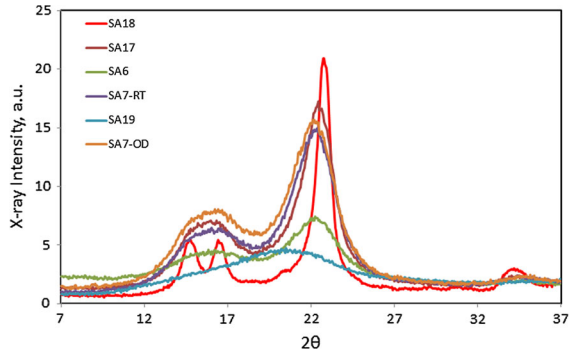

Fig. 3 WAXS diffractograms of some cellulose, wood, and treated wood samples

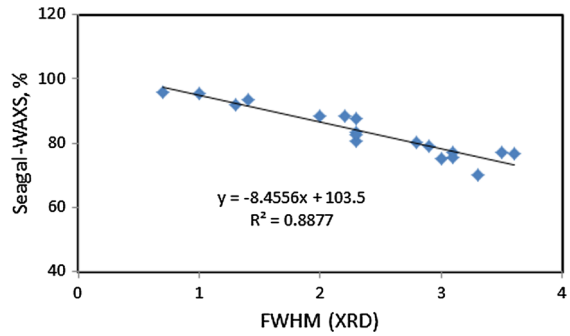

Fig. 4 Correlation between FWHM (XRD) and crystallinity (Segal-WAXS)

wherein cellulose was disordered (Lindner et al. 2014). The theoretical analysis concluded that microfibrils without any crystalline segments can lead to XRD peaks and thereby indicate the nature of disordered cellulose as crystalline. It must be noted that some of these results from models have yet to be substantiated by experiment, but we think that more caution is warranted in using WAXS for determining cellulose crystallinity. Therefore, the finding that the cell wall fibrils are non-crystalline not only explains the accessibility of D_2O to cellulose but also explains the broadened nature of the X-ray diffractograms.

Considering that both the 1380 cm^{-1} band intensity increase in Raman (D_2O caused, Table 2) and FWHM (X-ray diffraction, Table 4) were representative of DOLO, the two ought to be related. When this data was plotted for eight samples that were common in Tables 2 and 4, there was a nice correlation between the Raman intensity increase and the XRD FWHM (Fig. 5, $R^2 = 0.95$). This correlation further supported the view that indeed in XRD FWHM represented the degree of order (or disorder) between cellulose chains and suggested that FWHM may have less to do with other factors that are traditionally believed to be the cause (i.e., crystallite size, hemicellulose, lignin, irregularity of the crystal lattice, or amorphous cellulose). This is an interesting finding and needs further investigation.

It is reported in literature (Nishiyama et al. 2012) that, in crystalline materials, changes in FWHM (XRD) are related to change in the size of the crystallites. Therefore, in certain circumstances, a FWHM change may be interpretable in terms of both changes—DOLO and crystallite size change. To avoid this confusion, it is suggested that to determine if any FWHM (XRD) change observed in any cellulose material is solely due to a change in crystallite size, an OH-to-OD exchange based Raman experiment be performed (to calculate 1380 cm^{-1} band intensity change). If no change in the band intensity occurs beyond what is expected from the surface chains (Table SI1) that would imply changes to the crystallite size only. However, in case the change is more than the surface effect, consideration of a DOLO change may be appropriate.

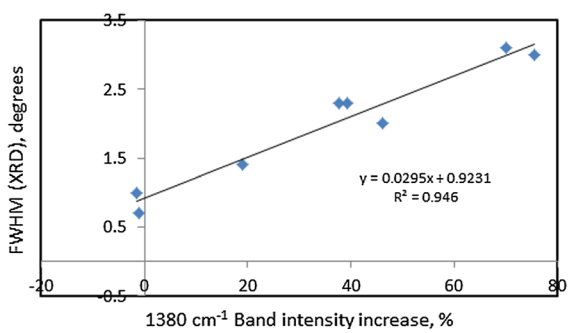

Fig. 5 Correlation between D_2O exchange caused Raman intensity increase at 1380 cm^{-1} and FWHM of [200] peak in X-ray diffraction

New model

Based on the information from this work, a new tentative model of cell wall cellulose is proposed (Fig. 6). In this model, along an individual cellulose chain, there are two types of sections—water accessible (curved line section with H–O–H next to it, Fig. 6) and water inaccessible (straight vertical line segment with no H–O–H present next to it, Fig. 6). Moreover, the Figure displays some areas that contain the symbol "?" next to H–O–H. This symbol designates the uncertainty about water's presence. On the right-hand side in Fig. 6, two such microfibrils are represented. The authors are cognizant that this model remains rudimentary and requires further development and testing.

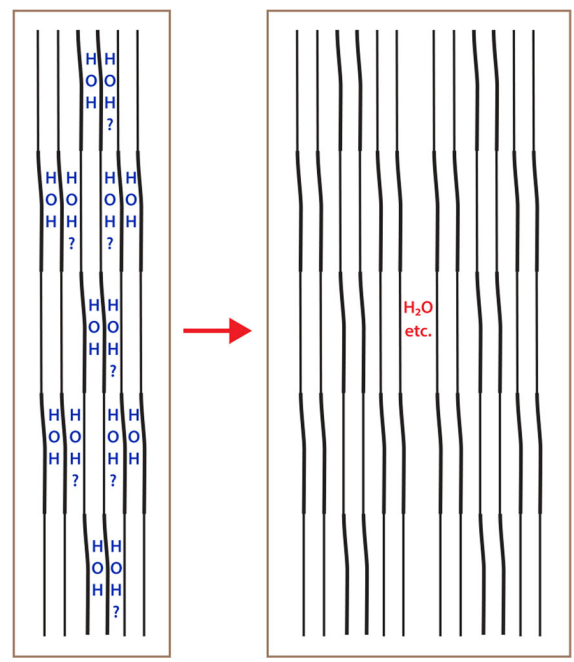

Fig. 6 Tentative model of cell wall cellulose based on the work described here

Interpretation of literature NMR data

Reported ^{13}C solid state NMR data can be explained based on the findings of the present investigation and the proposed cellulose microfibril model (Fig. 6). In terms of our model (Fig. 6), the 89 and 84 ppm peaks in ^{13}C NMR spectrum of cellulose can be assigned to water-inaccessible and water accessible C4s, respectively. Traditionally, in semi-crystalline cellulose, the peaks have been assigned to interior and surface C4 in cellulose (Wickholm et al. 1998; Atalla and VanderHart 1999; Wikberg and Maunu 2004). The C6 NMR region (60–68 ppm), on the other hand, still represents the *tg* and the *gt* conformations of the CH_2OH (Horii et al. 1983). Nevertheless, the *tg* and *gt* peaks (at ~66 and ~64 ppm, respectively) need to be reinterpreted in terms of C6s in water-inaccessible and water-accessible segments, respectively (Fig. 6) instead of crystalline and surface C6s (Wickholm et al. 1998; Atalla and VanderHart 1999; Wikberg and Maunu 2004).

In the following, a couple of examples from the literature are considered. In the case of mung bean cell walls NMR spectra (Newman et al. 2013, Bootten et al. 2004), under our model (Fig. 6) the 89 and 84 ppm peaks (Bootten et al. 2004, see Fig. 4 in this reference) would be due to the C4s in water- inaccessible and accessible segments of the chains, respectively. Similarly, in the C6 region, the ~66 and ~64 ppm signals represent the *tg* and *gt* conformations present in water-inaccessible and water-accessible segments, respectively (Fig. 6). In another investigation where microstructural changes of wood cellulose by moist-thermal treatments were reported (Kuribayashi et al. 2015), ^{13}C solid state NMR spectra of control (green beech wood) was compared with that of 200 °C heated wood. In the NMR spectrum of the latter, the peak in the C4 region at ~89 ppm intensified compared to the control whereas the peak intensity at ~84 ppm declined compared to control. Although, traditionally, the 89 and 84 ppm peaks have been assigned to the interior (crystalline) and surface cellulose C4s, respectively, under our model, the interpretation would be in terms of C4s being present in water-inaccessible and water-accessible regions (Fig. 6). Moreover, according to the model, explanation of the finding by Kuribayashi et al. (2015) would be that heating the wood to 200 °C resulted in the conversion of the water-accessible regions to water-inaccessible regions. This is supported by our recent findings (Agarwal et al. 2015) where water accessibility to cellulose of never-dried NaOH treated red pine holocellulose (SA7, Table 1) was reduced by 50 % upon oven drying (110 °C for 15 h). Additionally, this interpretation gets support from the corresponding change in the C6 region (Kuribayashi et al. 2015, see Fig. 4) where compared to the signal at 66 ppm, a decline in the intensity of the signal at 64 ppm (due to *gt* CH_2OH conformation) was observed when the NMR spectra of heated and control woods were compared. Conversion of the water-accessible segments to water-inaccessible segments in cellulose chains causes transformation of the local CH_2OH conformation from *gt* to *tg* (Table 3). Changes in the C4 region that were similar to those reported by Kuribayashi et al. (2015) have been previously published by other investigators (Wikberg and Maunu 2004). It was reported that cellulose crystallinity increased in thermally modified softwoods and hardwoods.

Conclusions

Our findings indicated that the interiors of never-dried wood cell wall microfibrils are accessible to water and that in turn implied that the fibrils cannot be crystalline. Moreover, upon thermal and/or chemi-thermal treatment the fibril structure consolidated and resulted in reduced accessibility to water. The finding of fibrils being non-crystalline was further supported by the observations of existence of at least two conformers of the CH_2OH groups in cellulose chains. This has important implication for the interchain hydrogen bonds in cellulose because only the *tg* conformation can participate in intra-plane, interchain H-bond formation. Additionally, the fact that low frequency Raman spectra did not contain any contribution from the microfibrils in their native state provided additional support for the fibrils being non-crystalline.

A new non-crystalline model of the microfibrils was proposed would account for the observation that no CNCs could be produced from either unmodified wood or from the holopulp before thermal treatment. This model also allowed us to rationalize the X-ray diffraction data obtained on a number of materials that were investigated in this study.

Acknowledgments The authors thank Dr. Akira Isogai (Tokyo University) for providing Tunicate and *Cladophora* celluloses. We acknowledge Fred Matt of the FPL Analytical Chemistry and Microscopy Laboratory Unit for carrying out the composition analyses of the samples. They extend their gratitude to Dr. J. Y. Zhu (FPL) for providing samples of untreated and SPORL-treated Douglas fir used in this work. The authors are grateful to Dr. Alfred French for the editorial review of the manuscript. The authors gratefully acknowledge use of X-ray facilities and instrumentation supported by NSF through the University of Wisconsin Materials Research Science and Engineering Center (DMR-1121288).

References

Agarwal UP (2006) Raman imaging to investigate ultrastructure and composition of plant cell walls: distribution of lignin and cellulose in black spruce wood (*Picea mariana*). Planta 224:1141–1153

Agarwal UP (2014) 1064 nm FT-Raman spectroscopy for investigations of plant cell walls and other biomass materials. Front Plant Sci 5:490

Agarwal UP, Ralph SA (1997) FT-Raman spectroscopy of wood: identifying contributions of lignin and carbohydrate polymers in the spectrum of black spruce (*Picea mariana*). Appl Spectrosc 51:1648–1655

Agarwal UP, Reiner RS, Ralph SA (2010) Cellulose I crystallinity determination using FT–Raman spectroscopy: univariate and multivariate methods. Cellulose 17:721–733

Agarwal UP, Reiner RS, Ralph SA (2013a) Estimation of cellulose crystallinity of lignocelluloses using near-IR FT-Raman spectroscopy and comparison of the Raman and Segal-WAXS methods. J Agric Food Chem 61:103–113

Agarwal UP, Zhu JY, Ralph SA (2013b) Enzymatic hydrolysis of loblolly pine: effects of cellulose crystallinity and delignification. Holzforschung 67:371–377

Agarwal UP, Ralph SA, Reiner RS, Stark NM (2015) Formation of irreversible H-bonds in cellulose materials. In: Hell J, Bohmdorfer S, Potthast A, Rosenau T (eds) Proceedings 18th international symposium on wood, fiber and pulping chemistry, BOKU Dept. Chemistry, Vienna, Vol II, pp 18–21

Atalla RH, Agarwal UP (1985) Raman microprobe evidence for lignin orientation in the cell walls of native woody tissue. Science 227:636–638

Atalla RH, Isogai A (2005) Recent developments in spectroscopic and chemical characterization of cellulose. In: Dumitriu S (ed) Polysaccharides: structural diversity and functional versatility. Marcel Dekker, New York, pp 125–157

Atalla RH, VanderHart DL (1999) The role of solid state ^{13}C NMR spectroscopy in studies of the nature of native celluloses. Solid State Nucl Magn Reson 15:1–19

Atalla RS, Crowley MF, Himmel ME, Atalla RH (2014) Irreversible transformations of native celluloses, upon exposure to elevated temperatures. Carbohydr Polym 100:2–8

Bali G, Foston MB, O'Neill HM, Evans BR, He J, Ragauskaus AJ (2013) The effect of deuteration on the structure of bacterial cellulose. Carbohydr Res 374:82–88

Bootten TJ, Harris PJ, Melton LD, Newman RH (2004) Solid-state ^{13}C-NMR spectroscopy shows that the xyloglucans in the primary cell walls of mung bean (*Vigna radiata* L.) occur in different domains: a new model for xyloglucan-cellulose interactions in the cell wall. J Exp Bot 55:571–583

Chen P, Ogawa Y, Nishiyama Y, Bergenstråhle-Wohlert M, Mazeau K (2015) Alternative hydrogen bond models of cellulose II and III_I based on molecular force-fields and density functional theory. Cellulose 22:1485–1493

Colaianni SEM, Aubard J, Hansen SH, Nielsen OF (1995) Raman spectroscopic studies of some biochemically relevant molecules. Vib Spectrosc 9:111–120

Colombo L, Furic K (1971) Low frequency Raman spectrum of benzoic acid single crystals. Spectrochim Acta 27A:1778–1784

Cosgrove DJ (2005) Growth of the plant cell wall. Nat Rev Mol Cell Biol 6:850–861

Davis MW (1998) A rapid method for compositional carbohydrate analysis of lignocellulosics by high pH anion-exchange chromatography with pulse amperometric detection (HPAE/PAD). J Wood Chem Technol 18:235–252

Ding SY, Himmel ME (2006) The maize primary cell wall microfibril: a new model derived from direct visualization. J Agric Food Chem 5:597–606

Donaldson L (2007) Cellulose microfibril aggregates and their size variation with cell wall type. Wood Sci Technol 41:443–460

Driemeier C, Pimenta MT, Rocha GJ, Oliveira MM, Mello DB, Maziero P, Gonçalves AR (2011) Evolution of cellulose crystals during prehydrolysis and soda delignification of sugarcane lignocellulose. Cellulose 18:1509–1519

Elazzouzi-Hafraoui S, Nishiyama Y, Putaux J-L, Heux L, Dubreuil F, Rochas C (2008) The Shape and size distribution of crystalline nanoparticles prepared by acid hydrolysis of native cellulose. Biomacromolecules 9:57–65

Fernandes AN, Thomas LH, Altaner CM, Callow P, Forsyth VT, Apperley DC, Kennedy CJ, Jarvis MC (2011) Nanostructure of cellulose microfibrils in spruce wood. Proc Natl Acad Sci USA 108:E1195–E1203

French AD, Santiago Cintron M (2013) Cellulose polymorphy, crystallite size, and the Segal crystallinity index. Cellulose 20:583–588

Gierlinger N, Luss S, Konig C, Konnerth J, Eder M, Fratzl P (2010) Cellulose microfibril orientation of Picea abies and its variability at the micron-level determined by Raman imaging. J Exp Bot 61:587–595

Hendra PJ, Jones C, Warnes G (1991) Fourier transform Raman spectroscopy. Ellis Horwood, Chicester

Hirota M, Tamura N, Saito T, Isogai A (2010) Water dispersion of cellulose II nanocrystals prepared by TEMPO-mediated oxidation of mercerized cellulose at pH 4.8. Cellulose 17:279–288

Horii F, Hirai A, Kitamaru R (1983) Solid-state 13C-NMR study of conformations of oligosaccharides and cellulose—

conformation of CH_2OH group about the exo-cyclic C–C bond. Poly Bull 10:357–361
Hult EL, Iversen T, Sugiyama J (2003) Characterization of the supermolecular structure of cellulose in wood pulp fibres. Cellulose 10:103–110
Jarvis MC (2013) Cellulose biosynthesis: counting the chains. Plant Physiol 163:1485–1486
Kafle K, Lee CM, Shin H, Zoppe J, Johnson DK, Kim SH, Park S (2015) Effects of delignification on crystalline cellulose in lignocellulose biomass characterized by vibrational sum frequency generation spectroscopy and X-ray diffraction. Bioenergy Res. doi:10.1007/s12155-015-9627-9
Keplinger T, Konnerth J, Aguié-Béghin V, Rüggeberg M, Gierlinger N, Burgert I (2014) A zoom into the nanoscale texture of secondary cell walls. Plant Methods 10:1
Kuramae R, Saito T, Isogai A (2014) TEMPO-oxidized cellulose nanofibrils prepared from various plant holocelluloses. React Funct Polym 85:126–133
Kuribayashi T, Ogawa Y, Nishiyama Y, Heux L, Saito Y, Matsumoto Y (2015) Microstructural changes of cellulose in wood by moist-thermal treatment. In: Hell J, Bohmdorfer S, Potthast A, Rosenau T (eds) Proceedings 18th international symposium on wood, fiber and pulping chemistry, BOKU Dept. Chemistry, Vienna, Vol I, pp 225–228
Langan P, Petridis L, O'Neill HM, Pingali SV, Foston M, Nishiyama Y, Schulz R, Lindner B, Hanson BL, Harton S, Heller WT, Urban W, Evans B, Gnanakaran S, Ragauskas AJ, Smith JC, Davison BH (2014) Common processes drive the thermochemical pretreatment of lignocellulosic biomass. Green Chem 16:63–67
Largo-Gosens A, Hernández-Altamirano M, García-Calvo L, Alonso-Simón A, Álvarez J, Acebes JL (2014) Fourier transform mid infrared spectroscopy applications for monitoring the structural plasticity of plant cell walls. Front Plant Sci 5:303
Lee CM, Kafle K, Park YB, Kim SH (2014) Probing crystal structure and mesoscale assembly of cellulose microfibrils in plant cell walls, tunicate tests, and bacterial films using vibrational sum frequency generation (SFG) spectroscopy. Phys Chem Chem Phys 16:10844–10853
Leu S-Y, Zhu JY, Gleisner R, Sessions J, Marrs G (2013) Robust enzymatic saccharification of a Douglas-fir forest harvest residue by SPORL. Biomass Bioenergy 59:393–401
Liitia T, Maunu SL, Hortling B, Tamminen T, Pekkala O, Varhimo A (2003) Cellulose crystallinity and ordering of hemicelluloses in pine and birch pulps as revealed by solid-state NMR spectroscopic methods. Cellulose 10:307–316
Lindner B, Petridis L, Langan P, Smith JC (2014) Determination of cellulose crystallinity from powder diffraction diagrams. Biopolymers 103:67–73
Liu J, Inouye H, Venugopalan N, Fischetti RF, Gleber SC, Vogt S, Cusumano JC, Kim JI, Chapple C, Makowski L (2013) Tissue specific specialization of the nanoscale architecture of Arabidopsis. J Struct Biol 184:103–114
Martínez-Sanz M, Gidley JG, Gilbert EP (2015) Application of X-ray and neutron small angle scattering techniques to study the hierarchical structure of plant cell walls: a review. Carbohydr Polym 125:120–134
Moon RJ, Martini A, Nairn J, Simonsen J, Youngblood J (2011) Cellulose nanomaterials review: structure, properties and nanocomposites. Chem Soc Rev 40:3941–3994
Newman RH (1999) Estimation of the lateral dimensions of cellulose crystallites using ^{13}C NMR signal strengths. Solid State Nucl Magn Reson 15:21–29
Newman RH (2008) Simulation of X-ray diffractograms relevant to the purported polymorphs cellulose IV_I and IV_{II}. Cellulose 15:769–778
Newman RH, Hill SJ, Harris PJ (2013) Wide-angle X-ray scattering and solid-state nuclear magnetic resonance data combined to test models for cellulose microfibrils in mung bean cell walls. Plant Physiol 163:1558–1567
Nishiyama Y, Johnson GP, French AD (2012) Diffraction from nonperiodic models of cellulose crystals. Cellulose 19:319–336
Nishiyama Y, Langan P, O'Neill H, Pingali SV, Harton S (2014) Structural coarsening of aspen wood by hydrothermal pretreatment monitored by small- and wide-angle scattering of X-ray and neutrons on oriented specimens. Cellulose 21:1015–1024
Okita Y, Saito T, Isogai A (2010) Entire surface oxidation of various cellulose microfibrils by TEMPO-mediated oxidation. Biomacromolecules 11:1696–1700
Park S, Baker JO, Himmel ME, Parilla PA, Johnson DK (2010) Cellulose crystallinity index: measurement techniques and their impact on interpreting cellulase performance. Biotechnol Biofuels 3:10
Parrott EJ et al (2009) Testing the sensitivity of terahertz spectroscopy to changes in molecular and supramolecular structure: a study of structurally similar cocrystals. Cryst Growth Des 9:1452–1460
Preston RD (1974) The physical biology of plant cell walls. Chapman and Hall, London
Ragauskas AJ, Williams CK, Davison BH, Britovsek G, Cairney J, Eckert CA, Frederick WJ Jr, Hallett JP, Leak DJ, Liotta CL, Mielenz JR, Murphy R, Templer R, Tschaplinski T (2006) The path forward for biofuels and biomaterials. Science 311:484–489
Reiner RS, Rudie AW (2013) Process scale-up of cellulose nanocrystal production to 25 kg per batch at the Forest Products Laboratory. In: Postek MT, Moon RJ, Rudie AJ, Bilodeau MA (eds) Production and applications of cellulose materials. TAPPI Press, Atlanta, pp 21–24
Reza M, Ruokolainen J, Vuorinen T (2014) Out-of-plane orientation of cellulose elementary fibrils on spruce tracheid wall based on imaging with high-resolution transmission electron microscopy. Planta 240:565–573
Saito T, Kimura S, Nishiyama Y, Isogai A (2007) Cellulose nanofibers prepared by TEMPO-mediated system. Biomacromolecules 8:2485–2491
Schenzel K, Fischer S, Brendler E (2005) New method for determining the degree of cellulose I crystallinity by means of FT Raman spectroscopy. Cellulose 12:223–231
Sèbe G, Ham-Pichavant F, Ibarboure E, Lydie A, Koffi C, Tingaut P (2012) Supramolecular structure characterization of cellulose II nanowhiskers produced by acid hydrolysis of cellulose I substrates. Biomacromolecules 13:570–578
Segal L, Creely JJ, Martin AE, Conrad CM (1959) An empirical method for estimating the degree of crystallinity of native cellulose using the x-ray diffractometer. Text Res J 29:786–794
Sun Q, Foston M, Meng X, Sawada D, Pingali SV, O'Neill HM, Li H, Wyman CE, Langan P, Ragauskas AJ, Kumar R

(2014) Effect of lignin content on changes occurring in poplar cellulose ultrastructure during dilute acid pretreatment. Cellulose 21:2419–2431

TAPPI test method (1983) Acid insoluble lignin in wood and pulp; official test method T-222 (Om). TAPPI, Atlanta, GA

Thomas LH, Forsyth VT, Martel A, Grillo I, Altaner CM, Jarvis MC (2014) Structure and spacing of cellulose microfibrils in woody cell walls of dicots. Cellulose 21:3887–3895

Vieira FS, Pasquini C (2014) Determination of cellulose crystallinity by terahertz-time domain spectroscopy. Anal Chem 86:3780–3786

Wickholm K, Larsson PT, Iversen T (1998) Assignment of non-crystalline forms in cellulose I by CP/MAS ^{13}C NMR spectroscopy. Carbohydr Res 312:123–129

Wikberg H, Maunu SL (2004) Characterisation of thermally modified hard- and softwoods by ^{13}C CPMAS NMR. Carbohydr Res 58:461–466

Wiley JH, Atalla RH (1987) Band assignments in the Raman spectra of celluloses. Carbohydr Res 160:113–129

Xu X, Liu F, Jiang L, Zhu JY, Haagenson D, Wiesenborn DP (2013) Cellulose nanocrystals vs. Cellulose nanofibrils: a comparative study on their microstructures and effects as polymer reinforcing agents. ACS Appl Mater Interfaces 5:2999–3009